Recycling rice husks for high-capacity lithium battery anodes

Dae Soo Jung[a,b,1], Myung-Hyun Ryou[a,1], Yong Joo Sung[c], Seung Bin Park[b], and Jang Wook Choi[a,2]

[a]Graduate School of Energy Environment Water Sustainability (World Class University) and KAIST Institute NanoCentury and [b]Department of Chemical and Biomolecular Engineering, Korea Advanced Institute of Science and Technology, Yuseong Gu, Daejeon 305-701, Korea; and [c]Department of Bio-Based Materials, Chungnam National University, Yuseong Gu, Daejeon 305-764, Korea

Edited by Stephen J. Harris, General Motors, Warren, MI, and accepted by the Editorial Board June 7, 2013 (received for review March 15, 2013)

The rice husk is the outer covering of a rice kernel and protects the inner ingredients from external attack by insects and bacteria. To perform this function while ventilating air and moisture, rice plants have developed unique nanoporous silica layers in their husks through years of natural evolution. Despite the massive amount of annual production near 10^8 tons worldwide, so far rice husks have been recycled only for low-value agricultural items. In an effort to recycle rice husks for high-value applications, we convert the silica to silicon and use it for high-capacity lithium battery anodes. Taking advantage of the interconnected nanoporous structure naturally existing in rice husks, the converted silicon exhibits excellent electrochemical performance as a lithium battery anode, suggesting that rice husks can be a massive resource for use in high-capacity lithium battery negative electrodes.

Rice is one of the most widespread food crops for human sustenance (Fig. 1*A*). It is currently cultivated in about 75 countries, and more than one-third of the global population eats rice as a staple food. Its worldwide annual production amounts to ∼422 million metric tons (1). The cultivation of rice plants generates a waste product, so-called rice husks (RHs), and upon the complete harvest of rice, the content of the RH reaches ∼20 wt% of the entire rice kernel, a very large amount, considering the massive scale of global rice production. The utilization of RHs has been an extensive research topic for decades (2). However, practical applications of RHs have been limited to a narrow range of low-value agricultural items, such as fertilizer additives, stockbreeding rugs, and bed soil, because of their tough and abrasive properties (2). There is a large opportunity for further research targeting more valuable applications.

Although RHs contain a variety of components such as lignin, cellulose, and silica, the present study pays attention mainly to recycling of the silica component. It has been known (3, 4) that silica accounts for ∼15–20 wt% of the entire RHs (Fig. 1*B*, *Lower Inset*) and originates from monosilicic acid that is first introduced into rice plants through their roots and is then moved to the rigid outer epidermal walls of the plants where it is converted into silica. The silica in RHs plays an important role in protecting rice from external attack by insects and bacteria (3, 5, 6), but simultaneously facilitates ventilation between inside and outside RHs to preserve moisture and nutrients inside the kernels. To perform these critical dual functions, the silica in RHs has developed unique porous nanostructures through years of natural evolution.

In an effort to recycle RHs toward high-value applications, in the present investigation, the RH silica possessing unique nanostructures has been applied in high-capacity lithium ion battery (LIB) anodes by reducing the silica to silicon (Si). Si has recently attracted considerable attention as an LIB anode due to its unparalleled theoretical capacity around 4,000 mAh/g (7–9), which is about 10 times higher than that of conventional graphite anodes (∼370 mAh/g). The development of high-capacity Si anodes is expected to accelerate the emergence of more advanced hybrid electrical vehicles and portable electronic devices. Despite the promising feature associated with the high specific capacity, however, Si typically suffers from capacity fading during cycling. This severe drawback is attributed to the extraordinarily large volume change of Si alloys, up to 300% during charging and discharging processes. This leads to capacity-fading mechanisms such as fracture of the Si alloys (10, 11) and unstable solid electrolyte interphase (SEI) formation (12). By contrast, the RH-originated Si in the present study overcomes these issues by using its unique interconnected porous nanostructure. Even though a number of nanostructured Si materials have been demonstrated (13–15) as high-performance LIB anodes, the nanostructured Si from RHs is substantially different, for the naturally defined structures existing in living organisms are directly used. Moreover, the readily available amount (∼10^7 tons) (1) of the RH-originated Si from worldwide cultivation is at least several orders of magnitude larger than the current demand for LIB anode raw materials (∼10^4–10^5 tons) (16).

Results and Discussion

The rice used in the current study was harvested from the suburbs of Daejeon in the Republic of Korea during September 2012. Characterization by optical microscopy reveals the morphology of RHs: The inner RH epidermis has a smooth surface, whereas the outer epidermis has a rough surface with repeated ridges (Fig. 1*B*, *Upper Inset*, and Fig. 1*C*). An elemental mapping analysis using energy dispersive spectroscopy (EDS) indicates that the silica is mainly concentrated at the tips of the outer surface (Fig. 1*C*, *Lower Inset* and Fig. S1). A more microscopic characterization of the concentrated silica region using scanning electron microscopy (SEM) showed that, in natural RHs, silica exists in the form of nanoparticles that are interconnected to constitute a porous structure (Fig. S1*B*). As summarized in Fig. 1*D*, during the overall synthetic procedure, the original RHs were first pretreated to extract high-purity silica, which was then reduced to generate the final Si. The detailed synthetic step and its yield are summarized in Fig. S2.

A thermal gravimetric analysis (TGA) verifies that silica indeed occupies 19.5 wt% of RHs (Fig. 2*A*). In the TGA data, the mass decreases in the temperature ranges of ∼175–350 °C and ∼380–550 °C correspond to decomposition of cellulose and lignin, respectively (17). In our experiment, we removed the 81.4 wt% of other organic and metal components through purification steps consisting of acid and heat treatments. Briefly, RHs were first leached with 10% (wt/vol) hydrochloric acid (HCl) and were then heat-treated at 650 °C for 3 h. See *Materials and Methods* for

Author contributions: D.S.J., S.B.P., and J.W.C. designed research; D.S.J. and M.-H.R. performed research; D.S.J., M.-H.R., and Y.J.S. analyzed data; and D.S.J., M.-H.R., and J.W.C. wrote the paper.

The authors declare no conflict of interest.

This article is a PNAS Direct Submission. S.J.H. is a guest editor invited by the Editorial Board.

[1]D.S.J. and M.-H.R. contributed equally to this work.

[2]To whom correspondence should be addressed. E-mail: jangwookchoi@kaist.ac.kr.

This article contains supporting information online at www.pnas.org/lookup/suppl/doi:10.1073/pnas.1305025110/-/DCSupplemental.

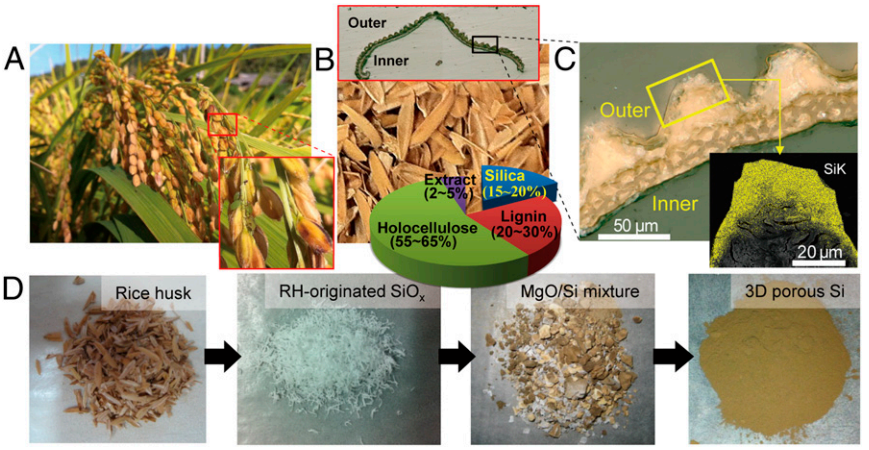

Fig. 1. Generation of 3D nanoporous Si from a rice plant. (*A*) Photographs of rice plant. (*B*) Photograph of rice husks obtained after milling. (*Upper Inset*) Optical microscope image showing the morphological characteristic of outer/inner surfaces of a rice husk. (*Lower Inset*) Circular chart indicating the composition of rice husks. (*C*) Optical microscope image of a rice husk shell magnified from the black box in *B*. (*Inset*) Si-mapped SEM-EDS image suggesting that Si exists mostly along the outer rugged surfaces of rice husks. (*D*) A series of photographs summarizing the procedures of synthesizing nanostructured Si from rice husks. (*Left* to *Right*) Pretreated rice husks by an acid-leaching process, rice husk-originated silica by a thermal decomposition process, a Si/MgO mixture formed after a magnesiothermic reduction process, and the final 3D porous Si obtained after an additional two-stage acid etching process.

details. After these pretreatments, according to inductively coupled plasma (ICP) analysis (Fig. 2*B*), the purity of the silica reaches 99.92%, implying that most other residual components were removed completely. It should be noted that although a single step of heat treatment can also generate silica from RHs, the acid treatment is essential in the present study. With a heat treatment alone, the purity of silica reaches only 95.48% (Table S1) because some metal components still remain. The acid treatment should be used to remove these residual metals by the formation of water-soluble metal chlorides. More importantly, the acid treatment is critical in preserving the original porous nanostructure all the way to the final formation of Si, which is very crucial for the stable operation of Si anodes. The same synthetic procedure, but with no acid treatment, would generate Si with the porous nanostructure collapsed (SEM image in Fig. S3). This is attributed to the fact that residual metals (Na, Ca, K, etc.) can generate ternary oxides such as $Na_6Si_8O_{19}$ and $Na_2Si_2O_5$ via reactions with silica (18, 19) and can melt at ~780 °C (20, 21). The use of HCl may not be a critical issue for the scale-up of the given synthetic procedure because HCl treatments have been well adopted in various industrial productions (22, 23). On the other hand, the purity of 95.48% resulting from the heat treatment alone is substantially higher than those of the other silica resources, such as quartz, bentonite, and diatomaceous earth, which are prepared by similar procedures. This shows that rice plants have naturally developed a process for the production of high-purity silica in their RHs. In addition, an X-ray diffraction (XRD) pattern (Fig. 2*C*) of the pretreated RH silica exhibits a broad peak around $2\Theta = 22.5°$, which is characteristic of amorphous silica.

The pretreated RH silica preserves the unique 3D porous structure that originates from the outer epidermis of natural RHs and is also desirable for good performance of the Si anode. Fig. 2 *D* and *E* shows SEM images of the RH silica viewed from the outer surface of an RH at low and high magnifications, respectively. These images clearly confirm that the nanoporous

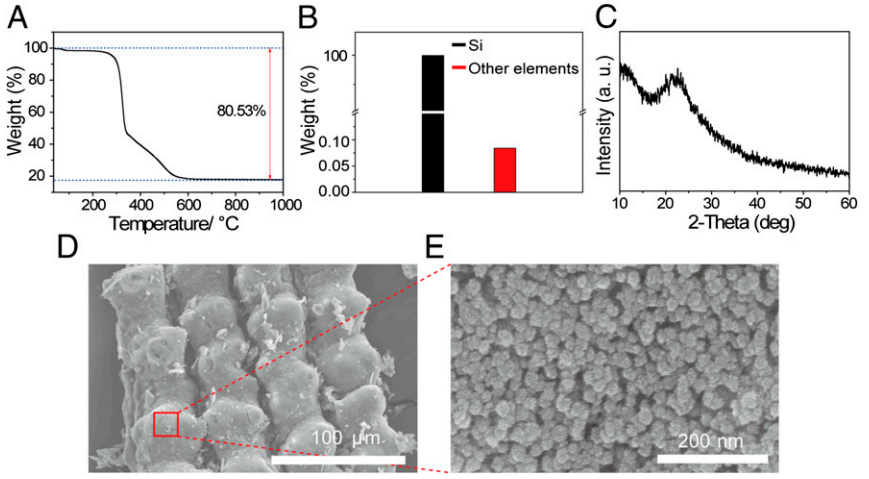

Fig. 2. Characterization of pretreated rice husk-originated silica. (*A*) A thermogravimetric analysis (TGA) curve of acid-leached rice husks indicating that the leached rice husks contain 19.5 wt% of silica. (*B*) Elemental analysis of the rice husk-originated silica after the acid-leaching and thermal treatment. Other elements include Al, B, Ba, Ca, Co, Cr, K, La, Li, Mn, Na, Ni, P, S, Ti, V, Zn, Zr, and Mg. (*C*) An XRD pattern of the rice husk-originated silica. (*D*) An SEM image of the rice husk-originated silica viewed from the outer surface. (*E*) The porous nanostructured silica magnified from the red box in *D*.

structure is well maintained in the pretreated RH silica. The porous nature of the pretreated RH silica was supported further by porosity measurements (Fig. S4*A*). Nitrogen adsorption–desorption experiments exhibit an isotherm that corresponds to type IV with a distinct hysteresis loop at high relative pressures (P/P_0), indicating that the pretreated RH silica is a mesoporous material. The Barrett–Joyner–Halenda (BJH) pore-size distribution showing a peak at 5 nm also supports the dominant presence of mesopores.

In an effort to transfer the desirable 3D porous structure of the RH silica to Si, a magnesiothermic reduction was carried out at 850 °C for 3 h. After the reduction, the converted Si retains similar bulk-scale morphology to that of the RH silica (Fig. 3*A*). However, the nanoporous structure of the RH silica was changed to an interconnected 3D porous wall structure (Fig. 3*B*), and this change was reflected in the decrease in the specific surface area (SSA) (286 → 47.3 m^2/g, Fig. S4 *A* and *B*). In the magnesiothermic reduction process, Si is produced through the following reaction: $SiO_{2(s)} + Mg_{(g)} \rightarrow Si_{(s)} + 2MgO_{(s)}$. In this reaction, solid magnesium (bp = 650 °C) functions as a reducing agent that first evaporates and then diffuses into SiO_2. Thus, in our samples, the Mg gas is able to get access to the surfaces deep inside the RH silica through the interconnected nanopores. As a result, a uniformly distributed Si/MgO mixture was produced (Fig. S5 *A*–*E*) without the formation of secondary phases like magnesium silicide (Mg_2Si) (Fig. S5*E*), in contrast to reports in the literature (24, 25). Even after selective removal of MgO by acid etching, the interconnected porous structure was observed, but, once again, the structure was changed, to an interconnected porous wall structure, which is attributed to the etching of MgO as well as grain growth during the high-temperature process. See the schematic illustration and corresponding SEM images in Fig. S5*F*.

The morphology and composition of the 3D porous Si were characterized further, using various analytical tools. The scanning transmission electron microscopy (STEM) and high-resolution transmission electron microscopy (HRTEM) images (Fig. 3 *C* and *D*) show clearly that the RH-originated Si has an interconnected porous wall structure with a wall thickness of ~13 nm and a pore diameter of 10~50 nm, which is indeed consistent with the pore size distribution result (Fig. S4*B*). The HRTEM image (Fig. 3*D*, *Lower Inset*) also shows lattice fringes corresponding to the Si (111) lattice, indicating the crystalline character of the 3D porous Si. The crystalline structure was also confirmed by

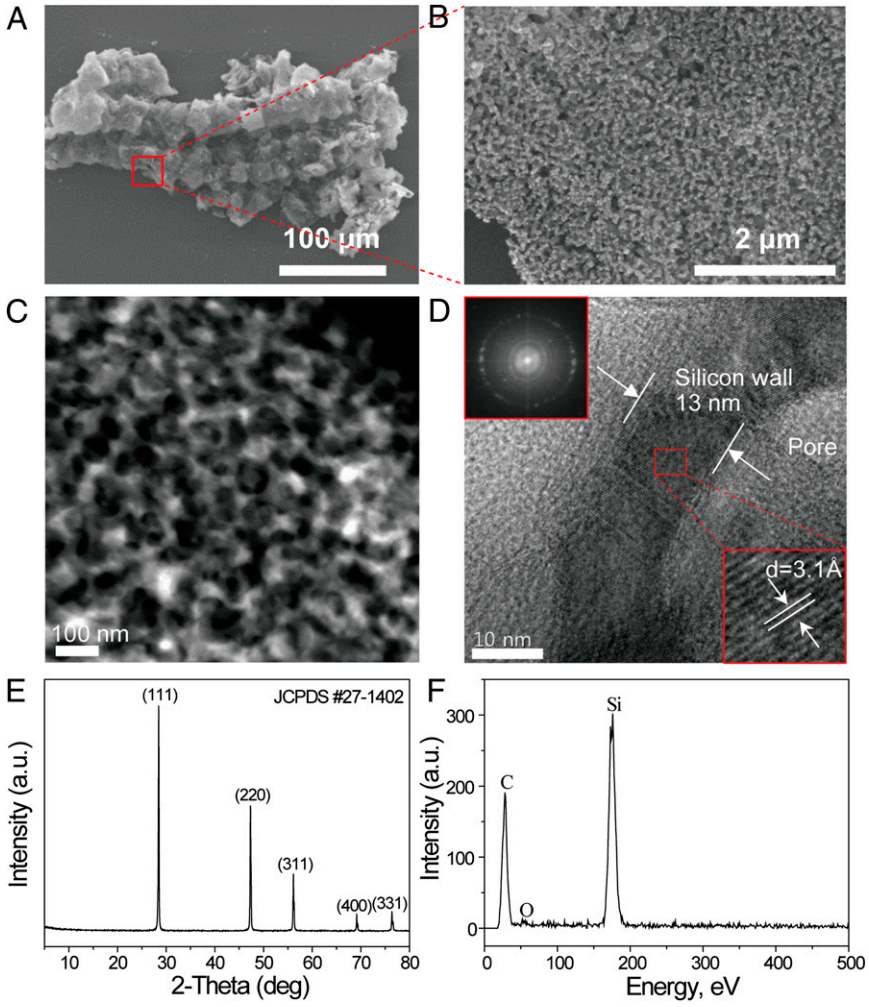

Fig. 3. Characterization of rice husk-originated Si. (*A* and *B*) SEM image (*A*) of rice husk-originated Si and its high-magnification image (*B*) magnified from the red box in *A*. (*C*) STEM image of the rice husk-originated Si exhibiting an interconnected 3D porous structure. (*D*) HRTEM image of the 3D porous Si wall structure. The Si wall thickness is ~13 nm. (*Upper Inset*) Selected area electron diffraction (SAED) showing a diffraction ring that corresponds to the (111) lattices of Si. (*Lower Inset*) HRTEM image showing the (111) lattice fringes with a *d*-spacing of 3.1 Å. (*E*) XRD pattern of the rice husk-originated Si with the major lattice orientations denoted. (*F*) Energy-dispersive X-ray spectrum of the rice husk-originated Si (carbon: sample holder line).

selected-area electron diffraction (SAED) (Fig. 3*D*, *Upper Inset*) that exhibits a diffraction ring corresponding to the Si (111) lattice. In addition, the XRD (Fig. 3*E*) and EDS (Fig. 3*F*) spectra verify the pure phase of the crystalline Si, as well as the complete removal of the MgO through the following reaction: $MgO + 2HCl \rightarrow MgCl_2 + H_2O$. From an ICP measurement, the purity of the 3D porous Si was found to be 99.5%, further confirming the formation of pure phase Si.

To evaluate the RH Si as a LIB anode, coin-type half-cells were prepared. See *Materials and Methods* for details. For this testing, we coated the RH Si with carbon layers to compensate for the intrinsically low electronic conductivity of Si as shown in previous studies (26–28). Also, having noted the critical effect of the carbon precursor on the properties of resultant coating layers (26), we chose polydopamine as a precursor material. It has been found that dopamine polymerization yields highly conformal polymer layers with a fine-tuning capability of the coating thickness (26, 28, 29). In the current investigation, after the polydopamine coating and subsequent carbonization, the coating thickness and carbon content were measured to be ∼3–10 nm and 12 wt%, respectively (Fig. S6). The Raman spectroscopy data (Fig. S6*D*) exhibit peaks at 1,360 cm^{-1} (D band, disordered) and 1,589 cm^{-1} (G band, graphene), suggesting an amorphous characteristic of the carbon layers. More importantly, the fine thickness control of the polydopamine layers fulfilled an important function, as the unique porosity of the RH Si was well maintained. Surface area measurements indicated that the carbon-coated Si had an SSA of 87 m^2/g and the pore size distribution with a major pore diameter of ∼10–50 nm was similar to that of the same sample before the carbon coating (Fig. S4*C*). Hereafter, we denote the carbon-coated RH Si as c-Si_{RH}.

The electrochemical testing of c-Si_{RH} was conducted primarily by galvanostatic measurements. Detailed measurement conditions are described in *Materials and Methods*. The first cycle shows the characteristic potential profile of crystalline Si (Fig. 4*A*). When measured at 0.1 C (1 C: 2,000 mA/g), lithiation and delithiation took place at 0.1 V and 0.42 V vs. Li/Li^+, respectively, and a reversible capacity of 1,615 mAh/g was observed. These values verify, again, the complete reduction of silica and the formation of pure Si. Remarkably, the first coulombic efficiency (CE) of c-Si_{RH} is 84.2%. Such excellent CE suggests that the interconnected porous structure enables the formation of stable SEI layers during the first cycle. Although carbon coating of Si has been known to improve the first CE in general (30), the present case of Si_{RH} exhibits an equally high first CE of 83.9% even before the carbon coating (Fig. S7*A*), implying that the interconnected nanoporous structure of Si_{RH} plays a major role for the high first CE. From control experiments (Fig. S7 *B* and *C*) based on bare carbonized polydopamine and Super P as well as their weight contents (8 and 20 wt%), it turns out that the capacity contributions from both carbonaceous additives are only 1% and 2%, respectively, of the total reversible capacity of c-Si_{RH} (= 1,615 mAh/g). See *SI Text* for detailed calculation.

Moreover, c-Si_{RH} shows excellent discharge capacity retention during cycling using the stable interconnected porous structure. As displayed in Fig. 4*B*, the cycling performance of c-Si_{RH} is clearly better than those of bare Si nanoparticles (NPs) and carbonized polydopamine-coated Si NPs (c-Si NPs). After 50 cycles, c-Si_{RH}, c-Si NPs, and Si NPs retain 100%, 36%, and 20% of their initial capacities, respectively. c-Si NPs show improved retention compared with the bare Si NPs, but are still inferior to c-Si_{RH}, perhaps because NP-to-NP connection and SEI layers in c-Si NPs still become unstable during cycling. Upon extended cycling, c-Si_{RH} continues to show outstanding capacity retention, as it retains 100% of the original capacity (1,554 mAh/g) after

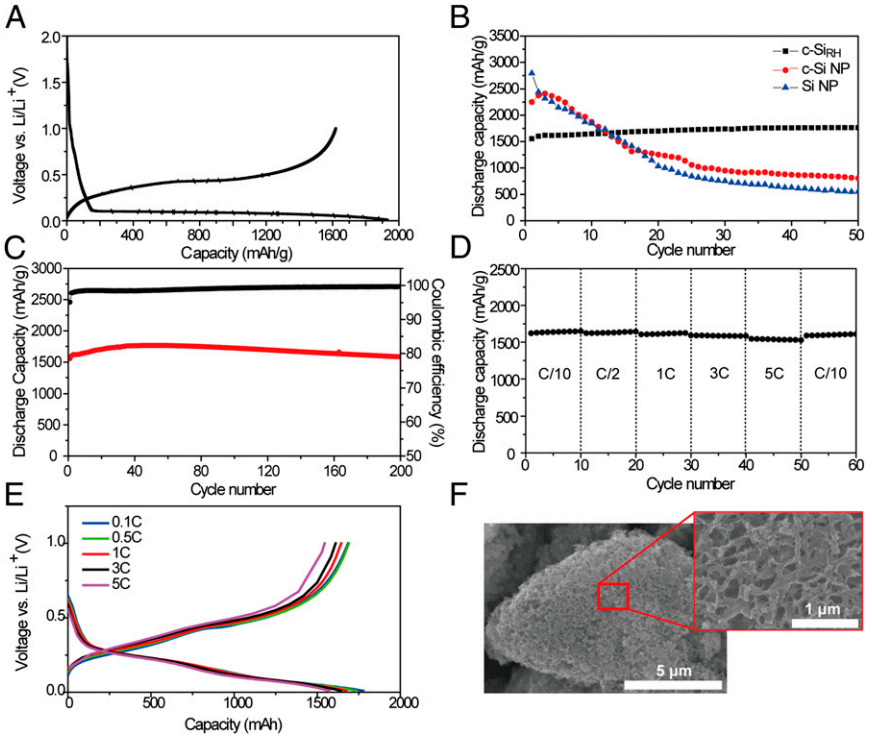

Fig. 4. (*A*) Voltage profiles in the first cycle measured at 0.1 C for the carbon-coated rice husk-originated Si (c-Si_{RH}) electrode. (*B*) Delithiation capacities of c-Si_{RH}, c-Si NPs, and bare Si NPs over cycling. (*C*) Delithiation capacities and CEs of c-Si_{RH}, cycled between 0.01 and 1.0 V vs. Li^+/Li. In both *B* and *C*, both charge and discharge were measured at a rate of 2 A/g (= 1 C). (*D* and *E*) Delithiation capacities (*D*) and voltage profiles (*E*) of c-Si_{RH} at various discharge rates from 0.1 C to 5 C (1 C = 2 A/g). The charge rate was fixed at 0.1 C. (*F*) SEM images of c-Si_{RH} after 50 cycles.

200 cycles when measured at a rate of 1 C (2,000 mA/g) (Fig. 4*C*). Also, the capacities and CEs during an additional 300 cycles measured at a higher rate of 3 C (6,000 mA/g) are presented in Fig. S8 *A* and *B*. During this cycling period, the capacity retention is 82%, and the average CE is 99.7%. These excellent capacity retentions suggest that the 3D interconnected porous structure originating from outer shells of natural RHs is advantageous and avoids the serious issues of Si anode deterioration, such as particle pulverization (12, 13, 31) and the formation of an unstable SEI (12, 32) that result from the repeated volume change of Si. Although the good capacity retentions of c-Si_{RH} could be attributed partially to the moderate mass loading of Si (~0.3 mg/cm^2), the clearly superior performance of c-Si_{RH} compared with that of c-Si NPs verifies the critical role of the interconnected nanoporous structure of Si_{RH} in the cycling performance. The superior cycling performance of c-Si_{RH} becomes more prominent when the mass loading of Si increases significantly by five times to ~1.5 mg/cm^2, as c-Si_{RH} retains 72% of the initial capacity after 100 cycles, but c-Si NPs retain only 23% even after 50 cycles (Fig. S8*C*).

Also, c-Si_{RH} shows good rate capability (Fig. 4*D*). To evaluate this, the charge rate was fixed at 0.2 A/g and the discharge rate was varied from 0.2 A/g to 10 A/g. Even when the discharge rate was increased 50 times from 0.1 C to 5 C, c-Si_{RH} retained 95.3% of the original discharge capacity (1,686 mAh/g) (Fig. 4*E*). This excellent rate performance is ascribed to the presence of a uniform carbon coating associated with polydopamine layers, as well as to the small wall thickness of the porous structure that facilitates efficient electronic and ionic diffusion. The SEM image of the c-Si_{RH} electrode taken after 50 cycles exhibits the well-maintained interconnected porous structure, verifying the robust nature of the c-Si_{RH} electrode.

Conclusions

The present study demonstrates that rice husks, a major by-product in rice harvest, can be used to produce Si with an ideal porous nanostructure for use in high-capacity LIB anodes. Its interconnected nanoporous structure, developed via years of natural evolution for efficient cultivation of rice, can resolve important issues in Si anode operation, enabling excellent cycling and power performance. Given that annual rice production reaches hundreds of millions of tons on a global scale, the promising battery data herein show how a part of the waste from one of the most popular crops, rice husks, can be a resource that helps meet the ever-increasing demand for Si in advanced batteries.

Materials and Methods

Fabrication of 3D Nanoporous Si from Rice Husks. The RHs used in the current study were obtained as a by-product of rice harvested in the suburbs of Daejeon in the Republic of Korea. The RHs were used as raw materials. The RHs were leached with a 10% (wt/vol) HCl solution to remove alkali metal impurities. To remove organic components, a thermal treatment was performed at 650 °C for 3 h. After these two steps, high-quality RH-originated silica was produced. The reduction of the RH-originated silica was conducted by magnesiothermic reduction. For the reduction, 4 g of the pretreated silica and 3.24 g of magnesium were introduced into a silicon carbide crucible and were well mixed. The filled crucible was closed tightly in an argon-filled glove box and was then moved to a furnace. The reduction was carried out at a temperature of 850 °C for 3 h ($2Mg + SiO_2 \rightarrow 2MgO + Si$). After the Mg reduction, high-purity 3D porous silicon was generated by two-stage etching. The collected magnesia/silicon mixture was stirred in 1 M HCl solution (HCl:H_2O:EtOH ratio = 0.66:4.72:8.88 in molar ratio) for 5 h at room temperature to selectively remove MgO ($MgO + 2HCl \rightarrow MgCl_2 + H_2O$). The HCl-etched silicon was then treated in HF solution (HF:H_2O:EtOH = 1.05:1.11:6.45 in molar ratio) to remove residual silica. For carbon coating of the chemically etched 3D porous Si, the Si_{RH} were first coated with polydopamine, which was subsequently carbonized to form carbon-coating layers. For this step, 0.4 g of Si_{RH} was dispersed in 10 mM Tris buffer solution (pH 8.5, 200 mL) and was sonicated for 20 min. Next, 0.4 g of 2-(3,4-dihydroxyphenyl) ethylamine hydrochloride [dopamine hydrochloride, 98% (vol/vol); Aldrich] was added and stirred for 24 h in the presence of oxygen for polymerization of dopamine. Once the polymerization was completed, Si_{RH} were filtered and rinsed with double-deionized water (DDW) three times to remove residual monomers, which was followed by a drying step under vacuum at 70 °C for 24 h. Finally, the dried polydopamine-coated Si was thermal treated at 800 °C for 3 h for the carbonization.

Characterization of the Rice Husk-Originated Silica and Si. The cross-sectional morphologies of RHs were investigated using an optical microscope (Olympus BX-51). XRD [Rigaku; D/MAX-2500 (18 kW)] spectra were acquired using CuKα radiation (λ = 1.5418 Å) to analyze the crystal structures of the RH-originated silica and silicon. The morphologies of the RH-originated silica and silicon were characterized by field emission scanning electron microscopy (FESEM) (HITACHI, S-4800/UHR-SEM; FEI, Magellan 400) and HRTEM (FEI; Tecnai G2 F30). An EDS attached to the SEM and TEM apparatus was used for local elemental analyses. The silica weight portion in the pretreated RHs and the Si weight portion in the carbon-coated 3D porous Si (c-Si_{RH}) were obtained on the basis of TGA (NETZSCH; TG 209 F3) measurements. The nitrogen adsorption and desorption isotherms were attained using the Brunauer-Emmett-Teller (BET) (Micrometrics; ASAP2010) method after degassing the samples at 383 K for 5 h. The concentrations of impurities in the RH-originated silica and Si were measured using an ICP-mass spectrometer (PerkinElmer; 5300DV). Raman spectroscopy (excitation, 514 nm) (high-resolution dispersive Raman microscope, Horiba Jobin Yvon; LabRAM HR UV/vis/NIR) was used to investigate the characteristics of carbon-coating layers. To verify the robust structural nature of the electrodes after cycling, the coin cells were opened and the electrodes were thoroughly washed with acetonitrile inside a glove box. Then, the electrodes were transferred to a SEM holder and the holder was completely sealed to prevent exposure to air. The samples were exposed to air for <30 s during the transfer to the vacuum chamber of SEM.

Battery Testing of 3D Porous Si. For the electrode fabrication, slurries were prepared by dissolving 60 wt% c-Si_{RH}, 20 wt% Super P, and 20 wt% poly (acrylic) acid (PAA) (M_r = 3,000,000; Aldrich) in *N*-methyl-2-pyrrolidone (NMP). The slurries were cast onto a copper current collector (18-μm-thick Cu foil; Hohsen) by using the doctor blade technique. The loading of the active materials was 0.3 mg/cm^2. The cast electrodes were dried at 70 °C for 10 h and punched into circular discs for coin-cell fabrication. Lithium hexafluorophosphate ($LiPF_6$) solution (1 M) in a mixture of ethylene carbonate (EC) and diethyl carbonate (DEC) (EC:DEC = 1:1, vol/vol) with 5 wt% fluoroethylene carbonate (PANAX E-TEC) was used as the electrolyte. To test the electrochemical properties, 2,032 type coin cells were assembled in an argon-filled glove box with a dew point below –60 °C at 25 °C. The cells were assembled by sandwiching separators (polypropylene; Celgard 2400) with the Si electrodes (working electrodes) and lithium metal (Honjo; reference/counter electrode). The cells were electrochemically cycled between 0.01 and 1.0 V vs. Li/Li^+ at 0.2 A/g under a constant current mode for both charge and discharge in the first cycle and cycled at different current rates thereafter using a cycle tester (PNE Solution).

ACKNOWLEDGMENTS. We acknowledge the financial support from a National Research Foundation of Korea (NRF) grants funded by the Korean Ministry of Education and Science Technology (MEST) (NRF-2010-0029031 and NRF-2012-R1A2A1A01011970).

1. Estevez M, Vargas S, Castaño V, Rodriguez R (2009) Silica nano-particles produced by worms through a bio-digestion process of rice husk. *J Non-Cryst Solids* 355(14):844–850.
2. Sun L, Gong K (2001) Silicon-based materials from rice husks and their applications. *Ind Eng Chem Res* 40(25):5861–5877.
3. Ma JF, Yamaji N (2006) Silicon uptake and accumulation in higher plants. *Trends Plant Sci* 11(8):392–397.
4. Tamai K, Ma JF (2003) Characterization of silicon uptake by rice roots. *New Phytol* 158(3):431–436.
5. Epstein E (1994) The anomaly of silicon in plant biology. *Proc Natl Acad Sci USA* 91(1):11–17.
6. Ma JF, et al. (2006) A silicon transporter in rice. *Nature* 440(7084):688–691.
7. Bruce PG, Scrosati B, Tarascon JM (2008) Nanomaterials for rechargeable lithium batteries. *Angew Chem Int Ed Engl* 47(16):2930–2946.
8. Scrosati B, Hassoun J, Sun YK (2011) Lithium-ion batteries. A look into the future. *Energy Environ Sci* 4(9):3287–3295.
9. Zhou W, Upreti S, Whittingham MS (2011) High performance Si/MgO/graphite composite as the anode for lithium-ion batteries. *Electrochem Commun* 13(10):1102–1104.

10. Chen Z, Christensen L, Dahn JR (2003) Large-volume-change electrodes for Li-ion batteries of amorphous alloy particles held by elastomeric tethers. *Electrochem Commun* 5(11):919–923.
11. Key B, et al. (2009) Real-time NMR investigations of structural changes in silicon electrodes for lithium-ion batteries. *J Am Chem Soc* 131(26):9239–9249.
12. Wu H, et al. (2012) Stable cycling of double-walled silicon nanotube battery anodes through solid-electrolyte interphase control. *Nat Nanotechnol* 7(5):310–315.
13. Cho J (2010) Porous Si anode materials for lithium rechargeable batteries. *J Mater Chem* 20(20):4009–4014.
14. Magasinski A, et al. (2010) High-performance lithium-ion anodes using a hierarchical bottom-up approach. *Nat Mater* 9(4):353–358.
15. Yu Y, et al. (2010) Reversible storage of lithium in silver-coated three-dimensional macroporous silicon. *Adv Mater* 22(20):2247–2250.
16. Institute of Information Technology (2011) *LIB Related Study Program 11-12* (Institute of Information Technology, Tokyo).
17. Pijarn N, Jaroenworaluck A, Sunsaneeyametha W, Stevens R (2010) Synthesis and characterization of nanosized-silica gels formed under controlled conditions. *Powder Technol* 203(3):462–468.
18. Allendorf MD, Spear KE (2001) Thermodynamic analysis of silica refractory corrosion in glass-melting furnaces. *J Electrochem Soc* 148(2):B59–B67.
19. Besmann TM, Spear KE (2004) Thermochemical modeling of oxide glasses. *J Am Ceram Soc* 85(12):2887–2894.
20. Hessien M, Rashad M, Zaky R, Abdel-Aal E, El-Barawy K (2009) Controlling the synthesis conditions for silica nanosphere from semi-burned rice straw. *Mater Sci Eng B* 162(1):14–21.
21. Yazhenskikh E, Hack K, Müller M (2006) Critical thermodynamic evaluation of oxide systems relevant to fuel ashes and slags. Part 1: Alkali oxide–silica systems. *Calphad* 30(3):270–276.
22. Dufault R, et al. (2009) Mercury from chlor-alkali plants: Measured concentrations in food product sugar. *Environ Health* 8(1):2.
23. Migahed M, Nassar I (2008) Corrosion inhibition of Tubing steel during acidization of oil and gas wells. *Electrochim Acta* 53(6):2877–2882.
24. Bao Z, et al. (2007) Chemical reduction of three-dimensional silica micro-assemblies into microporous silicon replicas. *Nature* 446(7132):172–175.
25. Chen W, Fan Z, Dhanabalan A, Chen C, Wang C (2011) Mesoporous silicon anodes prepared by magnesiothermic reduction for lithium ion batteries. *J Electrochem Soc* 158(9):A1055–A1059.
26. Liu N, et al. (2012) A yolk-shell design for stabilized and scalable li-ion battery alloy anodes. *Nano Lett* 12(6):3315–3321.
27. Hu YS, et al. (2008) Superior storage performance of a Si@SiOx/C nanocomposite as anode material for lithium-ion batteries. *Angew Chem Int Ed Engl* 47(9): 1645–1649.
28. Liu R, et al. (2011) Dopamine as a carbon source: The controlled synthesis of hollow carbon spheres and yolk-structured carbon nanocomposites. *Angew Chem Int Ed Engl* 50(30):6799–6802.
29. Zhao Y, Liu X, Li H, Zhai T, Zhou H (2012) Hierarchical micro/nano porous silicon Li-ion battery anodes. *Chem Commun* 48(42):5079–5081.
30. Bang BM, Lee JI, Kim H, Cho J, Park S (2012) High-performance macroporous bulk silicon anodes synthesized by template-free chemical etching. *Adv Energy Mater* 2(7): 878–883.
31. Bang BM, Kim H, Song HK, Cho J, Park S (2011) Scalable approach to multi-dimensional bulk Si anodes via metal-assisted chemical etching. *Energy Environ Sci* 4(12):5013–5019.
32. Szczech JR, Jin S (2011) Nanostructured silicon for high capacity lithium battery anodes. *Energy Environ Sci* 4(1):56–72.